Particuology 115 (2026) 118–125

Contents lists available at ScienceDirect

Particuology

journal homepage: www.elsevier.com/locate/partic

Unveiling the size-dependent electro-chemo-mechanical failure mechanisms of silicon anodes in sulfide-based all-solid-state batteries

Shi-Jie Yang[a,b,1], Ao-Long Yue[a,b,1], Hong Yuan[a,b,c,*], Ming-Xuan Xu[a,b], Zi-Hao Zuo[a,b], Di-Chen Wu[b,c], Yao-Hui Zhu[b,c], Chen Ling[a,b], Jia-Qi Huang[a,b,c,**]

[a] School of Materials Science & Engineering, Beijing Institute of Technology, Beijing, 100081, China
[b] School of Interdisciplinary Science, Beijing Institute of Technology, Beijing, 100081, China
[c] School of Interdisciplinary Science, Beijing Institute of Technology, Zhuhai, 519088, China

HIGHLIGHTS

- Electrochemical performance of Si-anodes with different particle sizes.
- Establishing the interfacial structural evolution of Si anodes.
- Unveiling the electro-chemo-mechanical failure mechanisms of Si anodes.

GRAPHICAL ABSTRACT

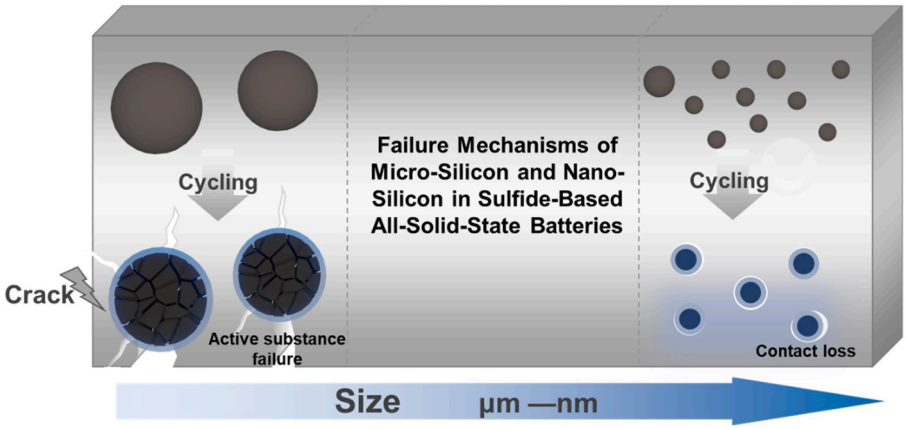

ARTICLE INFO

Keywords:
All-solid-state batteries
Silicon anode
Failure mechanisms
Particle size
Solid electrolyte interphase

ABSTRACT

High-capacity silicon anodes hold great promise for safe and energy-dense all-solid-state lithium batteries (ASSLBs), yet their practical application is hindered by interfacial degradation and mechanical fracture, which severely limit their cycle life. Herein, we unravel the particle-size-dependent electro-chemo-mechanical failure mechanisms of Si anodes in sulfide-based ASSLBs. The micro-sized Si (μm-Si) anode exhibits favorable initial Coulombic efficiency (ICE, 79.15%) and reversible capacity (2260.5 mAh g^{-1}) but succumbs to progressive particle fracture under prolonged cycling due to cumulative mechanical stress from large volume swings. By contrast, the nano-sized Si (nm-Si) anode suffers from severe interfacial side reactions and irreversible volume expansion due to its larger specific area and dense electrode structure, resulting in lower initial performance (ICE

This article is part of a special issue entitled: SI honoring Profs. Jin & Yu published in Particuology.

* Corresponding author. School of Materials Science & Engineering, Beijing Institute of Technology, Beijing 100081, China.
** Corresponding author. School of Materials Science & Engineering, Beijing Institute of Technology, Beijing 100081, China.
E-mail addresses: yuanhong@bit.edu.cn (H. Yuan), jqhuang@bit.edu.cn (J.-Q. Huang).

[1] The authors contributed equally to this work.

https://doi.org/10.1016/j.partic.2026.04.028
Received 2 April 2026; Received in revised form 28 April 2026; Accepted 29 April 2026
Available online 20 May 2026

of 72.21%, 1372.7 mAh g^{-1}). In subsequent cycles, the nm-Si anode experiences continuous interfacial side reactions, leading to substantial accumulation of interfacial decomposition byproducts and sustained capacity decay. These contrasting failure pathways establish electro-chemo-mechanical coupling as the governing principle and provide a particle-size-dependent design framework for high-performance Si-based ASSLBs.

1. Introduction

Energy density and safety together form the fundamental requirements for energy storage devices (Kim et al., 2023; Liao et al., 2025; Lin et al., 2017; Liu et al., 2023; Lv et al., 2026; Yang, Hu, Jiang, Yuan, et al., 2023; Yue et al., 2025). Sulfide-based all-solid-state lithium (Li) batteries (ASSLBs) have attracted considerable attention due to the non-flammability and high ionic conductivity of sulfide solid-state electrolytes (SSEs), which inherently address safety concerns while providing a solid foundation for high energy density (An et al., 2019; Cao et al., 2019, 2021; Feng et al., 2018; Man et al., 2023; Wang et al., 2025; Yang et al., 2024; Yang, Hu, Jiang, Cheng, et al., 2023). To further elevate energy density, the rising silicon (Si) anode offers a critical pathway. With its ultra-high theoretical specific capacity (~4200 mAh g^{-1}) (Cao et al., 2022; Pan, Xu, et al., 2022; Pan, Xu, et al., 2022; Ye et al., 2024), far surpassing that of traditional graphite anode (372 mAh g^{-1}), the Si anode holds great promise for unlocking the full potential of ASSLBs in future applications (Ge et al., 2021; Ham et al., 2024; Sun et al., 2025; Wang et al., 2022, 2024; Yang et al., 2022). However, the rapid capacity degradation of Si-based anode casts a shadow over their practical application (Adhitama et al., 2022; Gomez-Ballesteros & Balbuena, 2017; He et al., 2021; Zhou et al., 2019).

In general, Si anodes undergo significant volume expansion and shrinkage during reversible lithiation/delithiation (Li et al., 2021; Zhu et al., 2019). On one hand, the huge volume change of the Si anode during cycling induces significant stress and strain, leading to particle fracture, structural deterioration, and contact loss at the solid/solid interface within the composite electrode (Bai et al., 2022; Bonkile et al., 2023; Lin et al., 2015; McBrayer et al., 2021; Oh et al., 2022). On the other hand, the low operating potential of the Si anode triggers reductive decomposition of the sulfide SSEs at the interface, resulting in surface passivation and increased interfacial resistance (Domi et al., 2020; Kim et al., 2021; Li et al., 2024; Liao et al., 2023; Song et al., 2023; Wang et al., 2021). The coupling of these electro-chemo-mechanical effects gives rise to rapid capacity fading and short cycle life in Si-based ASSLBs (Huo et al., 2024; Wan et al., 2022; Wang et al., 2023; Yan et al., 2023). Nevertheless, the underlying coupled failure mechanisms remain poorly understood in all-solid-state systems, hindering the effective modulation of Si anode performance (Jiang et al., 2025).

Herein, we systematically reveal the size-dependent failure mechanisms of Si anodes by employing silicon anodes with different particle sizes in sulfide-based ASSLBs. Compared with nano-Si (nm-Si), the micro-Si (μm-Si) anode delivers a higher discharge specific capacity (2260.5 mAh g^{-1}) with a higher initial Coulombic efficiency (79.15%), benefiting from its low specific surface area, which suppresses interfacial side reactions and promotes favorable Li-ion diffusion kinetics. In contrast, the nm-Si anode suffers from severe interfacial side reactions due to its higher specific surface area, leading to increased interfacial impedance and consequently lower initial discharge capacity (1372.7 mAh g^{-1}) and Coulombic efficiency (72.21%). However, during prolonged cycling, the μm-Si anode undergoes rapid capacity decay, primarily attributed to stress concentration and mechanical fracture of μm-Si particles resulting from repeated large volume fluctuations. Conversely, the performance degradation of the nm-Si anode is dominated by interfacial side reactions, which show significant accumulation of interfacial byproducts. Collectively, these results reveal a size-dependent interplay of electro-chemo-mechanical coupling effects that governs the failure behavior of Si anodes in sulfide-based ASSLBs.

2. Methods

2.1. Materials

The Li foils (100 μm, 99.9%) and Cu foils (9 μm, 99.9%) were both purchased from China Energy Lithium Co., Ltd., Tianjin. The Li_6PS_5Cl (LPSCl) SSE powder was provided by Zhejiang Fengli New Energy Technology Co., Ltd. The Si powders were provided by Hongwu Technology Co., Ltd. Indium (In, 100 μm, 99.9%) foil was purchased from Qinghe County Fuxiang Metal Materials Co., Ltd. Carbon nanotubes (CNT) were obtained from Jiangsu Aikang Biomedical Research and Development Co., Ltd. All materials were kept in the glove box with oxygen and water contents below 1.0 ppm.

2.2. Preparation of Si-based ASSLBs

100 mg of LPSCl solid-state electrolyte powder was placed in the mould, and a pressure of 360 MPa was applied by a hydraulic machine for 1 min to complete the room-temperature pressing process of the electrolyte sheet.

The 3 mg of composite Si powder (60:30:10, Si:LPSCl:CNT by wt.%) was placed on one side of the mould and subjected to a pressure of 360 MPa for 3 min (Si mass loading of 2.3 mg cm^{-2}). In the half cell, Li or Li/In (prepared by cold-pressing a 100 μm thick Li foil and a 100 μm thick In foil together under a uniaxial pressure of 5 MPa for 1 min) were used as the counter electrode on the other side of the electrolyte sheet. The battery was subjected to a constant pressure of 10 MPa through a mechanical fastening device to ensure a tight contact between the electrode and the electrolyte interface. All operations were completed in an argon-protected glove box ($H_2O/O_2 < 0.1$ ppm), minimizing the interference of environmental factors on the stability of the interface.

2.3. Electrochemical measurements and material characterization

The Land CT2001 multichannel battery tester was used as the cell tester. All mould cells were assembled in an argon-filled glove box. Half-cell rate performance tests are conducted by gradually increasing the current (starting from 1 mA cm^{-2}). Electrochemical Impedance Spectroscopy (EIS) tests were performed using the Solartron 1470 E system (frequency range from 1 MHz to 0.1 Hz, amplitude of 10 mV). The DRT analyses were processed using the MATLAB GUI toolbox. Using stainless steel (SS)|Si-anode|SS cells to measure the electric conductivity of the composite Si anodes under an applied bias voltage of 10 mV. The ionic conductivity of the composite Si anode was calculated through EIS tests of SS|Si-anode|SS cells. The cyclic voltammetry (CV) tests of Li|LPSCl|Si cells were conducted within the voltage range from open circuit to −0.5 V (vs. Li/Li^+), with a sweep rate of 0.1 mV s^{-1} for two cycles. The pulsed current used by galvanostatic intermittent titration technique (GITT) tests of Li/In|LPSCl|Si cells was 1 mA cm^{-2}, the pulse duration is 5 min, and the relaxation time is 30 min. The constant current cycling tests were carried out using the LAND multi-channel battery testing system at a constant temperature of 25 °C.

X-ray photoelectron spectroscopy (XPS) measurements were conducted using an Al Kα X-ray source (1486.6 eV) with a linewidth of 0.68 eV. The XPS spectra were calibrated using the C 1s peak at 284.6 eV. The morphologies of the Si anode were characterized by scanning electron microscopy (SEM, JSM-7401 F, Japan) at 3.0 kV. The X-ray diffraction (XRD) patterns were obtained using the Bruker D8

Advance diffractometer (with Cu-Kα radiation, 40 kV, 120 mA). The pressure changes of Li/In|LPSCl|Si-anode cells were monitored through PSM-1CH (Beijing Zhongke Wanyuan Technology LTD) with an initial pressure of 185 MPa.

3. Results and discussion

3.1. Electrochemical performance of Si anodes with different particle sizes

Composite Si anodes were prepared by mixing different Si powders with LPSCl electrolyte and CNTs. The μm-Si and nm-Si powders exhibit average particle sizes of 4 μm and 100 nm, respectively (see Supplementary Fig. S1). XRD analysis of composite Si anodes reveals no detectable impurity phases beyond the signals of crystalline Si and the sulfide SSE (Fig. S2), confirming the good chemical compatibility between Si and the sulfide SSE during the preparation process.

To evaluate the electrochemical performance of the Si anodes with different particle sizes, Si||Li half cells were assembled and characterized. In terms of initial capacity and Coulombic efficiency, the μm-Si anode delivers an initial discharge capacity of 2260.5 mAh g^{-1} and an initial charge capacity of 1802.2 mAh g^{-1}, with an initial Coulombic efficiency (ICE) of 79.15%. In contrast, the nm-Si anode exhibits lower values of 1901.1 and 1372.7 mAh g^{-1}, corresponding to an ICE of 72.21% (Fig. 1a). Rate capability tests further reveal the superior capacity performance of μm-Si, which retains higher specific capacities of 1624.4, 1348.2, 1061.3, and 753.7 mAh g^{-1} at 0.1, 0.2, 0.5, and 1.0 C, respectively, compared with 1305.2, 1082.8, 819.0, and 574.1 mAh g^{-1} for nm-Si under the same conditions (Fig. 1b). The corresponding voltage-capacity curves further highlight the more pronounced capacity loss and voltage polarization in the nm-Si anode (Fig. 1c and d). Regarding long-term cycling stability, the μm-Si anode exhibits rapid capacity degradation, retaining only 11.5% of its initial capacity after 200 cycles, indicative of severe structural failure during prolonged operation (Fig. 1e). Conversely, despite a sharp capacity decline in the initial cycles (1st-50th cycle), the nm-Si anode shows a relatively stable subsequent cycling behavior (50th-200th cycle), achieving a capacity retention of 18.9% after 200 cycles (Fig. S3).

Taken together, the μm-Si anode delivers higher initial reversible capacity and superior rate performances yet suffers from rapid capacity fading upon extended cycling. In contrast, the nm-Si anode exhibits lower initial reversible capacity but achieves enhanced long-term cycling stability. These distinct electrochemical characteristics suggest fundamentally different degradation mechanisms depending on particle size between the two Si anodes, motivating a detailed mechanistic investigation into their respective failure processes.

3.2. Interfacial chemistry investigation

To elucidate the size-dependent failure mechanism, the Li^+ and electron transport behavior of Si anodes were systematically examined.

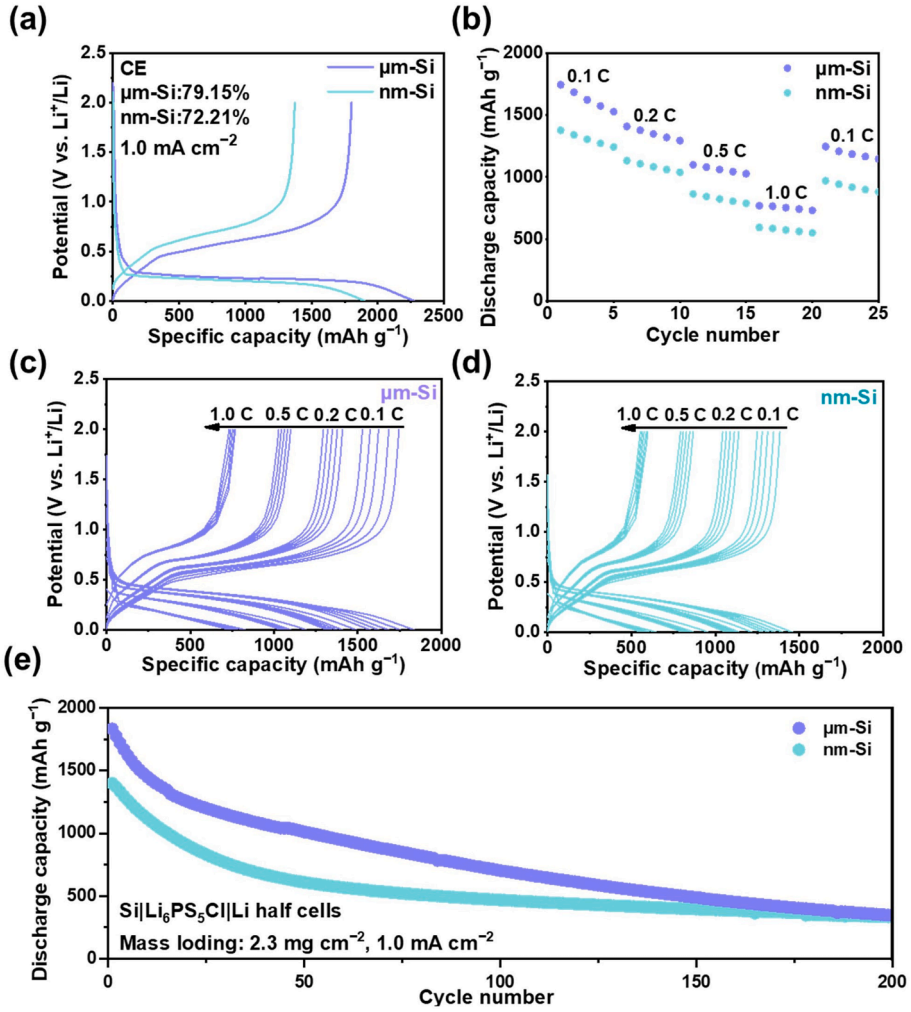

Fig. 1. Electrochemical performance of Si anodes with different particle sizes. (a) Galvanostatic charge and discharge profiles of μm-Si and nm-Si anodes at the initial cycle. (b) Rate performances and (c-d) corresponding charge and discharge profiles of μm-Si and nm-Si anodes (1.0 C = 5.7 mA cm^{-2}). (e) Long-cycling performances of μm-Si and nm-Si anodes at 1.0 mA cm^{-2}.

Firstly, the μm-Si anode shows both higher ionic conductivity (7.5 10^{-4} *vs.* 3.8 × 10^{-4} mS cm^{-1} of nm-Si) and electronic conductivity (9.6 10^{-4} *vs.* 1.9 × 10^{-4} mS cm^{-1} of nm-Si) before cycle (Fig. 2a). Galvanostatic intermittent titration technique (GITT) analysis confirms the lower polarization of μm-Si throughout the initial cycling (Fig. 2b). The detailed Li diffusion coefficient calculation further demonstrate faster ion transport within μm-Si (Fig. 2c). These results indicate that larger Si particle size facilitates a more continuous charge transport network within the composite Si anode, thereby enhancing the active material utilization.

The electrochemical stability of the Si/SSE interface was further examined to correlate particle size with the interfacial impedance. The μm-Si anode exhibits higher cycling reversibility than nm-Si during the initial cycles, suggesting more stable electrochemical reactions and fewer parasitic reactions (Fig. 2d and e). Corresponding electrochemical impedance spectroscopy (EIS) also reveals that the μm-Si anode exhibits a significantly lower interfacial impedance (11.7 Ω) compared with the nm-Si anode (16.1 Ω) after the first lithiation (Fig. 2f). This lower interfacial impedance further demonstrates the superior electrochemical stability of μm-Si (Fig. 2g).

X-ray photoelectron spectroscopy (XPS) analysis reveals that fewer decomposition products of sulfide SSE, mainly consisting of Li_2S and reduced phosphorus species (Ma et al., 2024), are present in μm-Si interface after the first lithiation process (Fig. 2h). In contrast, the nm-Si anode, with its larger specific surface area, accumulates a higher content of these decomposition products on its surface (Fig. 2i), indicative of increased parasitic interfacial side reactions that directly compromise its initial reversible capacity. The resulting Li_2S and reduced P species, both characterized by low Li^+ conductivity, further severely hinder Li^+ transport within the nm-Si anode and deteriorate its rate capability.

Collectively, the larger particle size of μm-Si establishes a more effective percolation network for ion/electron transport, while its lower specific surface area minimizes initial interfacial side reactions. This synergy underpins its higher initial reversible capacity and Coulombic efficiency. In contrast, the high specific surface area of nm-Si exacerbates parasitic interfacial reactions during the initial cycling, which significantly impedes charge transfer and degrades electrochemical performance. These distinct transport and interfacial characteristics provide a mechanistic insight into the initial performance difference, paving the way for further investigation into the structural evolution of the interface upon prolonged cycling.

To extend the interfacial analysis to long-term cycling and establish a link with the evolving electrochemical performance, we further probed the interfacial evolution and side reactions of the two Si anodes over extended cycles. From the perspective of interfacial kinetics evolution, in-situ EIS reveals a pronounced increase in interfacial impedance for nm-Si with cycling, consistent with the continuous formation of resistive surface layers and ongoing electrode degradation (Fig. 3a and b). Impedance fitting revealed a more rapid increase in both contact resistance (R_s) and charge-transfer resistance (R_{ct}) for the nm-Si anode during cycling compared to μm-Si (Fig. S4). This indicates significantly more severe interfacial side reactions in nm-Si, which in turn severely hindered interfacial ion/electron transport and degraded the anode's capacity. Distribution of relaxation time (DRT) analysis further resolves the evolution of individual interfacial processes, showing that within 15 cycles, the nm-Si anode experiences significant accumulation of

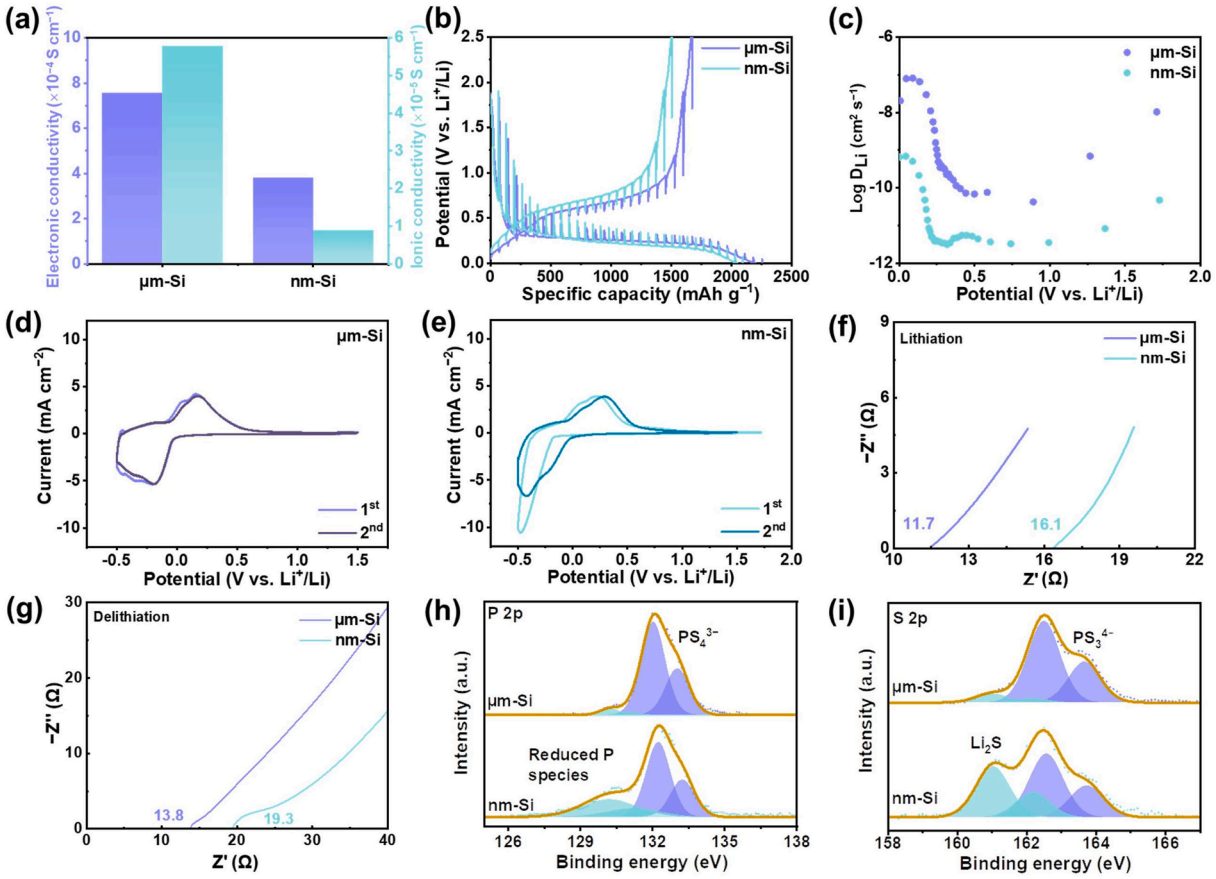

Fig. 2. Interfacial kinetics and interfacial chemistry of different Si anodes. (a) The ionic conductivity and electronic conductivity of μm-Si and nm-Si anodes. (b) GITT curves and (c) corresponding Li-ion diffusion coefficients of the Li|LPSCl|μm-Si cell and the Li|LPSCl|nm-Si cell at 1 mA cm^{-2}. (d, e) The CV curves of μm-Si and nm-Si anodes at the initial cycle using Li|LPSCl|Si configuration. The EIS curves of μm-Si and nm-Si anodes after the initial (f) lithiation and (g) delithiation processes. (h, i) XPS spectra of μm-Si and nm-Si anodes after the first cycle.

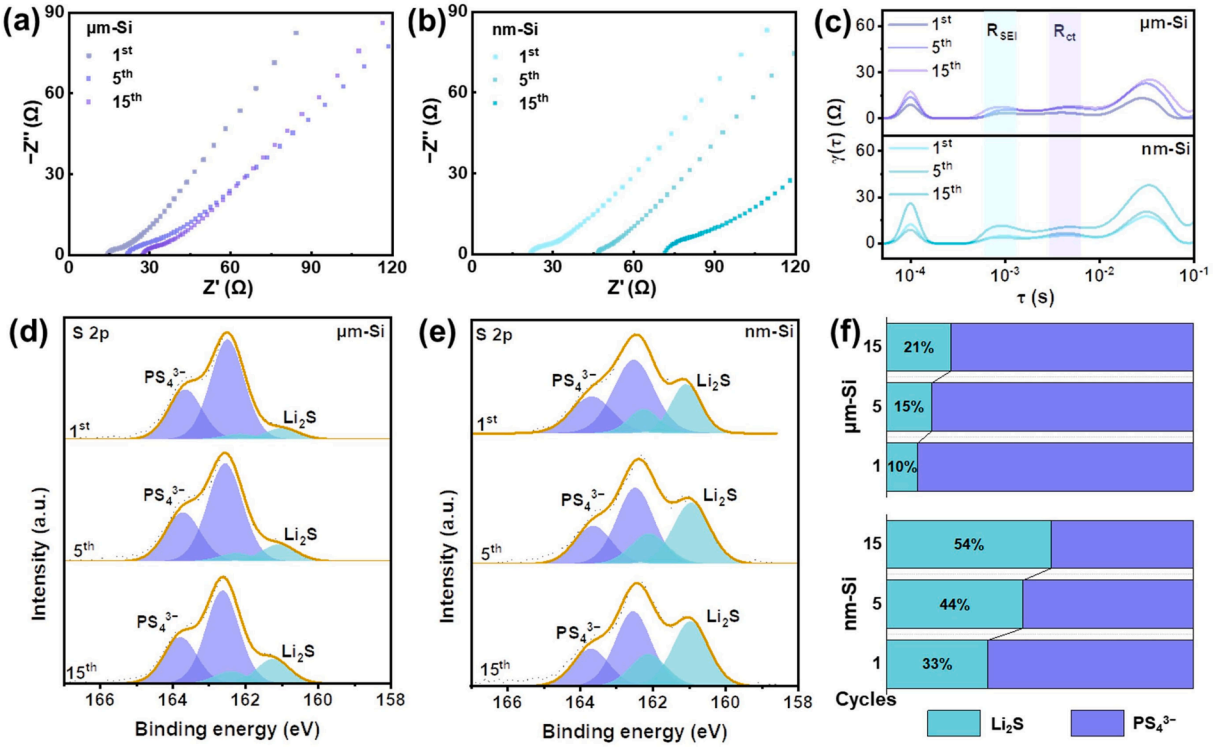

Fig. 3. Interfacial chemistry evolution. (a, b) EIS curves of Li|LPSCl|Si cells with μm-Si and nm-Si anodes after 1st, 5th, and 15th cycles. (c) The corresponding DRT curves of Li|LPSCl|Si cells at different cycle numbers. (d, e) XPS spectra of μm-Si and nm-Si anodes after different cycle numbers and (f) the corresponding percentage charts of the XPS spectra. The relative contents of different sulfur species were calculated based on their respective fitted peak areas relative to the total sulfur (S 2p) spectral area.

interfacial byproducts (reflected in the R_{SEI}) and progressive deterioration of charge transfer kinetics (R_{ct}, Fig. 3c). In stark contrast, the μm-Si anode exhibits a much slower rise in interfacial impedance, indicating superior interfacial stability during the initial cycling stage.

In terms of interfacial composition evolution, XPS analysis reveals that nm-Si already accumulates substantial Li_2S decomposition products (33%) within the initial cycle, reflecting the rapid onset of parasitic interfacial reactions (Fig. 3d and e). These side reactions consume active Li, contributing directly to irreversible capacity loss and early performance degradation. In contrast, μm-Si exhibits markedly suppressed side reactions during the initial cycle, with only 10% Li_2S detected. However, upon extended cycling (15 cycles), even the μm-Si anode begins to exhibit severe interfacial degradation, as evidenced by the accumulation of decomposition byproducts and a corresponding decline in reversible capacity. This result indicates that the interfacial side reactions play a significant role in the reduction of the capacity of the μm-Si anode.

Hence, the μm-Si anode combines intrinsically fast charge-transfer kinetics with superior initial interfacial stability relative to nm-Si, accounting for its higher initial capacity and rate capability. Regrettably, prolonged cycling progressively compromises the interfacial integrity of μm-Si anode, leading to increased side reactions and eventual capacity fade. These findings extend the understanding of particle-size-dependent interfacial chemistry from the initial to the long-term cycling regime, setting the stage for a detailed examination of the corresponding structural evolution within the Si electrodes.

3.3. Electrode structure and mechanical stress evolution

To further elucidate the particle-size-dependent failure mechanisms and extend the understanding beyond interfacial chemistry, we systematically tracked the structural evolution of composite Si anodes using ex situ SEM analysis across pristine, lithiated, and delithiated states (Fig. 4a and b). Regarding the initial lithiation/delithiation processes, the μm-Si anode exhibits larger pores due to its larger particle size, which serve as effective expansion buffers during lithiation. Conversely, the nm-Si anode initially presents a more compact structure, offering limited free volume to accommodate volume change (Fig. S5). Upon lithiation, both the μm-Si and nm-Si anodes transform into relatively uniform and dense structures due to the volume expansion. However, the μm-Si anode shows a thickness increase from 45.2 μm to 66.7 μm (147.6%, anode's thickness after delithiation/anode's pristine thickness), followed by a recovery to 50.0 μm upon delithiation (Fig. S6). The presence of larger pores in μm-Si provides void space to buffer volumetric expansion during lithiation (Fig. 4a). As a result, this effectively lowers the overall strain and reduces irreversible deformation, thereby contributing to better structural reversibility. In contrast, the nm-Si anode undergoes a more pronounced thickness variation, expanding from 25.9 μm to 50.0 μm (193.0%) during lithiation and only partially recovering to 43.7 μm during delithiation (Fig. 4b). The relatively compact packing of nm-Si particles provides insufficient free volume to accommodate lithiation-induced swelling, exacerbating mechanical stress during cycling. This results in a significantly larger irreversible thickness change of 17.8 μm for the nm-Si anode, compared to 4.8 μm for the μm-Si anode. The high irreversible structure change of nm-Si anode leads to severe active-Si isolation and capacity decrease at the initial cycle.

In terms of particle cracking and electrode structural integrity, subsequent SEM characterizations further confirm that nm-Si anode develops more extensive porosity after the initial delithiation process compared to μm-Si (Fig. 4c and d). Owing to the lack of accommodation space, the nm-Si anode mechanically fails to withstand lithiation-induced expansion, and the subsequent delithiation triggers significant structural collapse, which directly compromises its reversible capacity. Although μm-Si anode exhibited superior reversibility in volume change, prolonged cycling still induces particle cracking due to

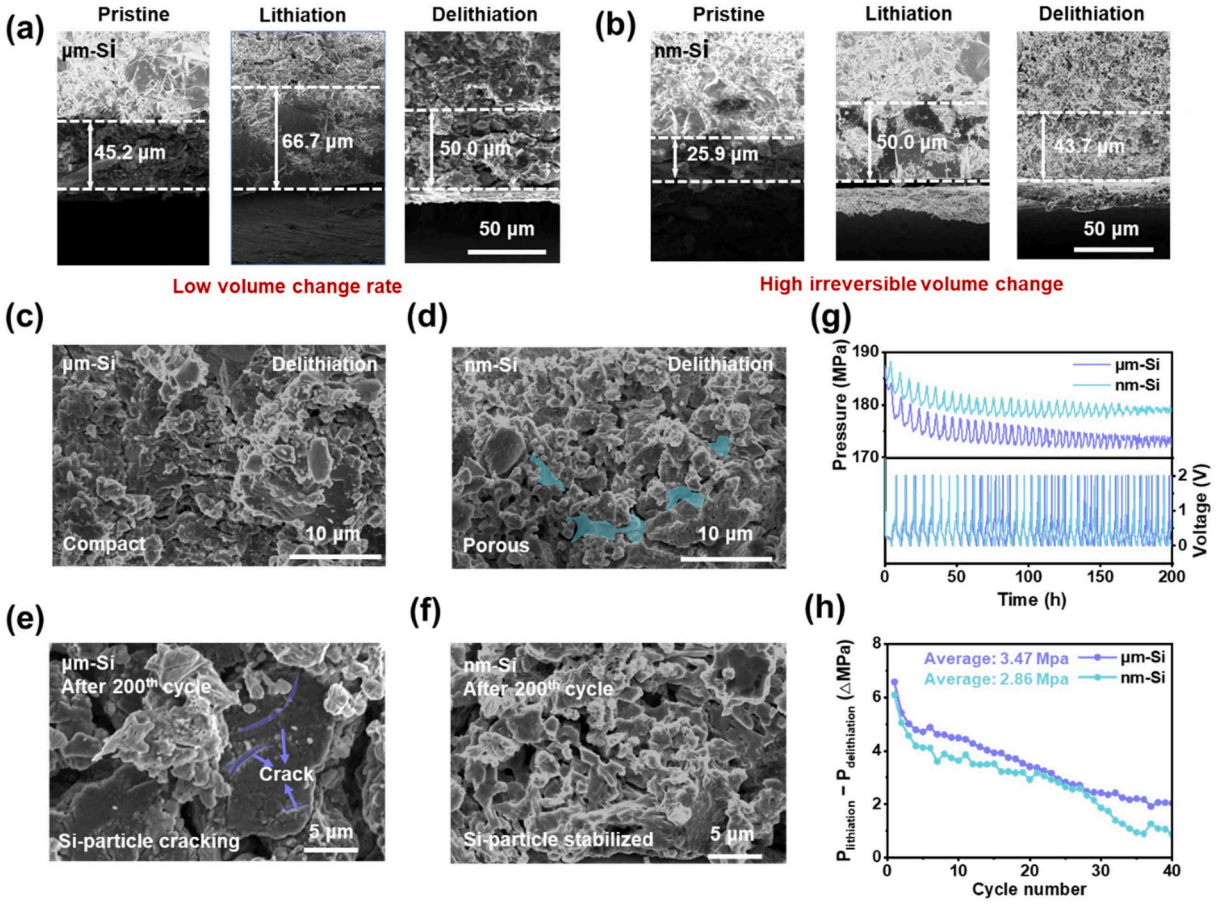

Fig. 4. Analysis of anode structure evolutions. (a, b) The cross-sectional SEM images of μm-Si and nm-Si anodes at the initial state, after the first lithiation, and after the first delithiation processes. (c, d) The surface SEM images of μm-Si and nm-Si anodes after the first delithiation process. (e, f) The SEM images of μm-Si and nm-Si anodes after 200 cycle. (g) The pressure variation and cycle curves of Li/In||Si cells at a current density of 1 mA cm^{-2} and (h) the corresponding pressure difference value between each lithiation ($P_{lithiation}$) and delithiation ($P_{delithiation}$) process of Li/In||Si cells.

recurrent strain accumulation, as revealed by post-cycling SEM (see Fig. 4e, f and Fig. S7).

To correlate structural degradation with mechanical stress evolution, in situ pressure measurements were conducted to monitor the dynamic stress variations throughout cycling (Fig. 4g and h). Persistent mechanical stress fluctuations corroborate the degradation mechanism of μm-Si anode under extended operation. The more severe volumetric expansion of μm-Si particles during each cycle leads to the accumulated mechanical stress. Under prolonged cycling with repeated pressure swings (3.47 Mpa of μm-Si anode compared to 2.86 Mpa of nm-Si anode), this stress buildup renders μm-Si particles prone to pronounced fragmentation and rapid capacity degradation within prolonger cycles. On the contrary, the limited volume variation of nm-Si particles in subsequent cycles helps preserve Si particle integrity, enabling its stable long-term capacity retention and cycling performance.

Overall, the electrochemical behavior and structural stability of Si anodes in sulfide-based ASSLBs are fundamentally governed by particle size, leading to distinct electro-chemo-mechanical failure pathways (Fig. 5). Electrochemically induced volume changes generate mechanical stress that disrupts solid-solid contacts, exposing fresh surfaces to trigger parasitic chemical reactions, which in turn further amplify electrochemical degradation. Therefore, the μm-Si anode offers higher initial capacity and rate capability due to its continuous ionic/electronic transfer network, porous buffer architecture and suppressed side reactions, but suffers from progressive particle cracking and rapid capacity fading under prolonged cycling. In contrast, the nm-Si anode exhibits

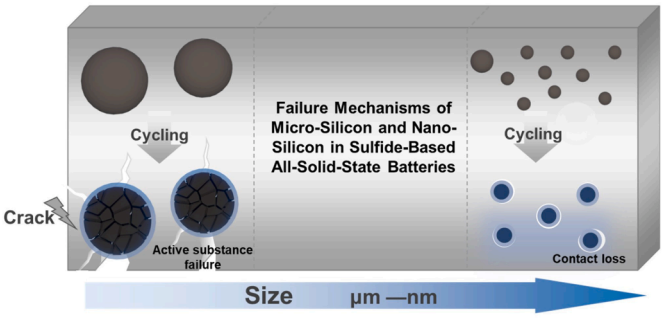

Fig. 5. Schematic of the size-dependent failure mechanisms of μm-Si and nm-Si anodes in ASSLBs.

severe initial degradation originating from drastic interfacial side reactions yet achieves better long-term stability owing to reduced volumetric fluctuations. These contrasting behaviors underscore the critical role of particle size in dictating the degradation mechanisms of Si-based ASSLBs, highlighting a fundamental trade-off between initial electrochemical performance and long-term structural stability. Based on the size-dependent electro-chemo-mechanical failure mechanisms, future efforts should be focused on designing bimodal or hierarchical particle size distributions to synergistically combine high initial capacity with long-term stability, developing stress-buffering electrode architectures, and employing operando characterization to unravel coupled failure mechanisms. Such strategies will guide the rational design of high-

energy-density, durable Si-based ASSLBs.

4. Conclusion

In summary, this work systematically unveils the particle-size-dependent electro-chemo-mechanical failure mechanisms of the Si anode in sulfide-based ASSLBs. The μm-Si anode benefits from its larger particle size, which provides a porous buffer architecture that effectively accommodates volume expansion during initial cycling, resulting in restrained side reactions, lower interfacial impedance, and superior structural reversibility. Consequently, μm-Si anode delivers the higher initial reversible capacity and rate capability. However, under prolonged cycling, cumulative mechanical stress from recurrent volume fluctuations induces the progressive cracking of μm-Si particles, which in turn exacerbates interfacial side reactions and ultimately drives rapid capacity fading. In contrast, the nm-Si anode, characterized by its high specific surface area and compact packing, suffers from severe interfacial side reactions and pronounced irreversible volume change during the initial cycle, leading to its significant structural collapse and rapid early capacity decay. Nevertheless, its limited volumetric fluctuations in subsequent cycles preserve the integrity of nm-Si particles, enabling the more stable long-term cycling performance. These contrasting behaviors establish a particle-size-dependent trade-off between the initial performance and long-term durability, providing critical design principles for high-performance Si-based all-solid-state batteries.

CRediT authorship contribution statement

Shi-Jie Yang: Writing – original draft, Investigation. **Ao-Long Yue:** Writing – review & editing, Investigation. **Hong Yuan:** Writing – review & editing, Supervision, Conceptualization. **Ming-Xuan Xu:** Validation, Investigation. **Zi-Hao Zuo:** Writing – review & editing, Investigation. **Di-Chen Wu:** Writing – review & editing, Validation, Investigation. **Yao-Hui Zhu:** Validation, Investigation. **Chen Ling:** Writing – review & editing. **Jia-Qi Huang:** Writing – review & editing, Supervision, Project administration, Funding acquisition, Conceptualization.

Declaration of competing interest

The authors declare that they have no known competing financial interests or personal relationships that could have appeared to influence the work reported in this paper.

Acknowledgments

This work was supported by the National Key Research and Development Program of China (grant No. 2021YFB2500300), the National Natural Science Foundation of China (grant Nos. 22479012, 224B2901), the Beijing Municipal Natural Science Foundation (grant No. L223009), the Hebei Natural Science Foundation (grant No. E2024208084).

Appendix A. Supplementary data

Supplementary data to this article can be found online at https://doi.org/10.1016/j.partic.2026.04.028.

References

Adhitama, E., Dias Brandao, F., Dienwiebel, I., Bela, M. M., Javed, A., Haneke, L., … Placke, T. (2022). Pre-lithiation of silicon anodes by thermal evaporation of lithium for boosting the energy density of lithium ion cells. *Advanced Functional Materials, 32*(22), Article 2201455. https://doi.org/10.1002/adfm.202201455

An, W., Gao, B., Mei, S., Xiang, B., Fu, J., Wang, L., … Huo, K. (2019). Scalable synthesis of ant-nest-like bulk porous silicon for high-performance lithium-ion battery anodes. *Nature Communications, 10*, 1447. https://doi.org/10.1038/s41467-019-09510-5

Bai, X., Yu, T., Ren, Z., Gong, S., Yang, R., & Zhao, C. (2022). Key issues and emerging trends in sulfide all solid state lithium battery. *Energy Storage Materials, 51*, 527–549. https://doi.org/10.1016/j.ensm.2022.07.006

Bonkile, M. P., Jiang, Y., Kirkaldy, N., Sulzer, V., Timms, R., Wang, H., … Wu, B. (2023). Coupled electrochemical-thermal-mechanical stress modelling in composite silicon/graphite lithium-ion battery electrodes. *Journal of Energy Storage, 73*, Article 108609. https://doi.org/10.1016/j.est.2023.108609

Cao, C., Abate, I. I., Sivonxay, E., Shyam, B., Jia, C., Moritz, B., … Toney, M. F. (2019). Solid electrolyte interphase on native oxide-terminated silicon anodes for Li-ion batteries. *Joule, 3*(3), 762–781. https://doi.org/10.1016/j.joule.2018.12.013

Cao, D., Sun, X., Li, Y., Anderson, A., Lu, W., & Zhu, H. (2022). Long-cycling sulfide-based all-solid-state batteries enabled by electrochemo-mechanically stable electrodes. *Advanced Materials, 34*(24), Article e2200401. https://doi.org/10.1002/adma.202200401

Cao, Z., Zheng, X., Qu, Q., Huang, Y., & Zheng, H. (2021). Electrolyte design enabling a high-safety and high-performance Si anode with a tailored electrode-electrolyte interphase. *Advanced Materials, 33*(38), Article 202103178. https://doi.org/10.1002/adma.202103178

Domi, Y., Usui, H., Ando, A., Nishikawa, K., & Sakaguchi, H. (2020). Analysis of the Li distribution in Si-based negative electrodes for lithium-ion batteries by soft X-ray emission spectroscopy. *ACS Applied Energy Materials, 3*(9), 8619–8626. https://doi.org/10.1021/acsaem.0c01238

Feng, K., Li, M., Liu, W., Kashkooli, A. G., Xiao, X., Cai, M., & Chen, Z. (2018). Silicon-based anodes for lithium-ion batteries: From fundamentals to practical applications. *Small, 14*(8), Article 1702737. https://doi.org/10.1002/smll.201702737

Ge, M., Cao, C., Biesold, G. M., Sewell, C. D., Hao, S.-M., Huang, J., … Lin, Z. (2021). Recent advances in silicon-based electrodes: From fundamental research toward practical applications. *Advanced Materials, 33*(16), Article 202004577. https://doi.org/10.1002/adma.202004577

Gomez-Ballesteros, J. L., & Balbuena, P. B. (2017). Reduction of electrolyte components on a coated si anode of lithium-ion batteries. *The Journal of Physical Chemistry Letters, 8*(14), 3404–3408. https://doi.org/10.1021/acs.jpclett.7b01183

Ham, S.-Y., Sebti, E., Cronk, A., Pennebaker, T., Deysher, G., Chen, Y.-T., … Meng, Y. S. (2024). Overcoming low initial coulombic efficiencies of Si anodes through prelithiation in all-solid-state batteries. *Nature Communications, 15*(1), 2991. https://doi.org/10.1038/s41467-024-47352-y

He, Y., Jiang, L., Chen, T., Xu, Y., Jia, H., Yi, R., … Wang, C. (2021). Progressive growth of the solid–electrolyte interphase towards the Si anode interior causes capacity fading. *Nature Nanotechnology, 16*(10), 1113–1120. https://doi.org/10.1038/s41565-021-00947-8

Huo, H., Jiang, M., Bai, Y., Ahmed, S., Volz, K., Hartmann, H., … Janek, J. (2024). Chemo-mechanical failure mechanisms of the silicon anode in solid-state batteries. *Nature Materials, 23*(4), 543–551. https://doi.org/10.1038/s41563-023-01792-x

Jiang, Z.-J., Luo, Z.-H., Guo, J.-X., Du, Y.-F., Jiang, F., Shen, N.-L., … Wu, Y. (2025). Thermal safety overview of silicon-carbon anode in lithium-ion batteries: Key parameters in determining the reactivity. *Particuology, 100*, 178–185. https://doi.org/10.1016/j.partic.2025.03.013

Kim, J., Chae, O. B., & Lucht, B. L. (2021). Perspective—Structure and stability of the solid electrolyte interphase on silicon anodes of lithium-ion batteries. *Journal of the Electrochemical Society, 168*(3), Article 030521. https://doi.org/10.1149/1945-7111/abe984

Kim, S., Park, G., Lee, S. J., Seo, S., Ryu, K., Kim, C. H., & Choi, J. W. (2023). Lithium-metal batteries: From fundamental research to industrialization. *Advanced Materials, 35*(43), Article e2206625. https://doi.org/10.1002/adma.202206625

Li, H., Guo, S., & Zhou, H. (2021). In-situ/operando characterization techniques in lithium-ion batteries and beyond. *Journal of Energy Chemistry, 59*, 191–211. https://doi.org/10.1016/j.jechem.2020.11.020

Li, S., Yang, S. J., Liu, G. X., Hu, J. K., Liao, Y. L., Wang, X. L., … Zhang, Q. (2024). A dynamically stable mixed conducting interphase for all-solid-state lithium metal batteries. *Advanced Materials, 36*(3), Article 2307768. https://doi.org/10.1002/adma.202307768

Liao, Y., Hu, J.-K., Fu, Z.-H., Zhao, C.-Z., Lu, Y., Li, S., … Yuan, H. (2023). Integrated interface configuration by in-situ interface chemistry enabling uniform lithium deposition in all-solid-state lithium metal batteries. *Journal of Energy Chemistry, 80*, 458–465. https://doi.org/10.1016/j.jechem.2023.02.012

Liao, Y. L., Wang, X. L., Yuan, H., Li, Y. J., Xu, C. M., Li, S., … Huang, J. Q. (2025). Ultrafast Li-rich transport in composite solid-state electrolytes. *Advanced Materials, 37*(10), Article 2419782. https://doi.org/10.1002/adma.202419782

Lin, D., Liu, Y., & Cui, Y. (2017). Reviving the lithium metal anode for high-energy batteries. *Nature Nanotechnology, 12*(3), 194–206. https://doi.org/10.1038/nnano.2017.16

Lin, D., Lu, Z., Hsu, P.-C., Lee, H. R., Liu, N., Zhao, J., … Cui, Y. (2015). A high tap density secondary silicon particle anode fabricated by scalable mechanical pressing for lithium-ion batteries. *Energy & Environmental Science, 8*(8), 2371–2376. https://doi.org/10.1039/c5ee01363a

Liu, H., Sun, Q., Zhang, H., Cheng, J., Li, Y., Zeng, Z., … Ci, L. (2023). The application road of silicon-based anode in lithium-ion batteries: From liquid electrolyte to solid-state electrolyte. *Energy Storage Materials, 55*, 244–263. https://doi.org/10.1016/j.ensm.2022.11.054

Lv, T.-T., Liu, J., He, L.-J., Wang, X.-L., Yang, S.-J., Zuo, Z.-H., … Yuan, H. (2026). Proton-regulated nitrite release enables anion-derived solid electrolyte interphase for stable lithium metal anodes. *Journal of Energy Chemistry, 116*, 38–46. https://doi.org/10.1016/j.jechem.2025.12.052

Ma, M., Du, M., Liu, Y., Lü, H., Yang, J., Hao, Z., … Wu, X. (2024). Electrode particulate materials for advanced rechargeable batteries: A review. *Particuology, 86*, 160–181. https://doi.org/10.1016/j.partic.2023.05.006

Man, Q., An, Y., Liu, C., Shen, H., Xiong, S., & Feng, J. (2023). Interfacial design of silicon/carbon anodes for rechargeable batteries: A review. *Journal of Energy Chemistry, 76*, 576–600. https://doi.org/10.1016/j.jechem.2022.09.020

McBrayer, J. D., Rodrigues, M.-T. F., Schulze, M. C., Abraham, D. P., Apblett, C. A., Bloom, I., … Cunningham, B. (2021). Calendar aging of silicon-containing batteries. *Nature Energy, 6*(9), 866–872. https://doi.org/10.1038/s41560-021-00883-w

Oh, P., Yun, J., Choi, J. H., Saqib, K. S., Embleton, T. J., Park, S., … Cho, J. (2022). Development of high-energy anodes for all-solid-state lithium batteries based on sulfide electrolytes. *Angewandte Chemie International Edition, 61*(25), Article e202201249. https://doi.org/10.1002/anie.202201249

Pan, S., Han, J., Wang, Y., Li, Z., Chen, F., Guo, Y., … Yang, Q.-H. (2022). Integrating sei into layered conductive polymer coatings for ultrastable silicon anodes. *Advanced Materials, 34*(31), Article 2203617. https://doi.org/10.1002/adma.202203617

Pan, H., Xu, Z., Wei, Z., Liu, X., Xu, M., Zong, C., … Wang, Q. (2022). Synergistic double cross-linked dynamic network of epoxidized natural rubber/glycinamide modified polyacrylic acid for silicon anode in lithium ion battery: High peel strength and super cycle stability. *ACS Applied Materials & Interfaces, 14*(29), 33315–33327. https://doi.org/10.1021/acsami.2c08038

Song, R., Yao, J., Xu, R., Li, Z., Yan, X., Yu, C., … Zhang, L. (2023). Metastable decomposition realizing dendrite-free solid-state Li metal batteries. *Advanced Energy Materials, 13*(9), Article 2203631. https://doi.org/10.1002/aenm.202203631

Sun, J. Y., Wang, Z. Y., Shen, X., Wu, Y., & Cheng, X. B. (2025). Thermal runaway mechanisms and mitigation strategies of silicon-based anode in lithium-ion batteries: A review. *Advanced Energy Materials, 16*(9), Article e05793. https://doi.org/10.1002/aenm.202505793

Wan, J., Yan, H.-J., Wen, R., & Wan, L.-J. (2022). In situ visualization of electrochemical processes in solid-state lithium batteries. *ACS Energy Letters, 7*(9), 2988–3002. https://doi.org/10.1021/acsenergylett.2c01069

Wang, X., Li, C., Chen, Z., & Sun, Y. (2024). Implantation of solid electrolyte interphase stabilizer within high-capacity silicon electrode enabling enhanced battery performance. *Energy Material Advances, 5*, 95. https://doi.org/10.34133/energymatadv.0095

Wang, X. L., Li, Y., Liu, J., Yang, S. J., Hu, J. K., Mai, W. Q., … Huang, J. Q. (2025). A robust dual-layered solid electrolyte interphase enabled by cation specific adsorption-induced built-in electrostatic field for long-cycling solid-state lithium metal batteries. *Angewandte Chemie International Edition, 64*(10), Article e202421101. https://doi.org/10.1002/anie.202421101

Wang, C., Liang, J., Zhao, Y., Zheng, M., Li, X., & Sun, X. (2021). All-solid-state lithium batteries enabled by sulfide electrolytes: From fundamental research to practical engineering design. *Energy & Environmental Science, 14*(5), 2577–2619. https://doi.org/10.1039/d1ee00551k

Wang, J.-C., Wang, P.-F., & Yi, T.-F. (2023). Challenges and optimization strategies at the interface between sulfide solid electrolyte and lithium anode. *Energy Storage Materials, 62*, Article 102958. https://doi.org/10.1016/j.ensm.2023.102958

Wang, C., Yang, C., & Zheng, Z. (2022). Toward practical high-energy and high-power lithium battery anodes: Present and future. *Advanced Science, 9*(9), Article 202105213. https://doi.org/10.1002/advs.202105213

Yan, W., Mu, Z., Wang, Z., Huang, Y., Wu, D., Lu, P., … Wu, F. (2023). Hard-carbon-stabilized Li-Si anodes for high-performance all-solid-state Li-ion batteries. *Nature Energy, 8*(8), 800–813. https://doi.org/10.1038/s41560-023-01279-8

Yang, S., Hu, J.-K., Jiang, F.-N., Cheng, X.-B., Sun, S., Hsu, H.-J., … Zhang, Q. (2023). Oxygen-induced thermal runaway mechanisms of Ah-level solid-state lithium metal pouch cells. *eTransportation, 18*, Article 100279. https://doi.org/10.1016/j.etran.2023.100279

Yang, S., Hu, J. K., Jiang, F. N., Yuan, H., Park, H. S., & Huang, J. Q. (2023). Safer solid-state lithium metal batteries: Mechanisms and strategies. *InfoMat, 6*(2), Article e12512. https://doi.org/10.1002/inf2.12512

Yang, S. J., Yao, N., Jiang, F. N., Xie, J., Sun, S. Y., Chen, X., … Zhang, Q. (2022). Thermally stable polymer-rich solid electrolyte interphase for safe lithium metal pouch cells. *Angewandte Chemie International Edition, 61*(51), Article e202214545. https://doi.org/10.1002/anie.202214545

Yang, S., Yuan, H., Yao, N., Hu, J. K., Wang, X. L., Wen, R., … Huang, J. Q. (2024). Intrinsically safe lithium metal batteries enabled by thermo-electrochemical compatible in situ polymerized solid-state electrolytes. *Advanced Materials, 36*(3), Article 2405086. https://doi.org/10.1002/adma.202405086

Ye, L., Lu, Y., Wang, Y., Li, J., & Li, X. (2024). Fast cycling of lithium metal in solid-state batteries by constriction-susceptible anode materials. *Nature Materials, 23*(2), 244–251. https://doi.org/10.1038/s41563-023-01722-x

Yue, A.-L., Yuan, H., Yang, S.-J., Hu, J.-K., Wang, X.-L., Wu, D.-C., … Huang, J.-Q. (2025). Amorphous fluorinated interphase enables fast Li-ion kinetics in sulfide-based all-solid-state lithium metal batteries. *Journal of Energy Chemistry, 107*, 277–284. https://doi.org/10.1016/j.jechem.2025.03.048

Zhou, F., Li, Z., Lu, Y.-Y., Shen, B., Guan, Y., Wang, X.-X., … Yu, S.-H. (2019). Diatomite derived hierarchical hybrid anode for high performance all-solid-state lithium metal batteries. *Nature Communications, 10*(1), 2482. https://doi.org/10.1038/s41467-019-10473-w

Zhu, M., Wu, J., Wang, Y., Song, M., Long, L., Siyal, S. H., … Sui, G. (2019). Recent advances in gel polymer electrolyte for high-performance lithium batteries. *Journal of Energy Chemistry, 37*, 126–142. https://doi.org/10.1016/j.jechem.2018.12.013